Designer Titania-Supported Au–Pd Nanoparticles for Efficient Photocatalytic Hydrogen Production

Ren Su,[†] Ramchandra Tiruvalam,[‡] Andrew J. Logsdail,[§] Qian He,[‡] Christopher A. Downing,[§] Mikkel T. Jensen,[⊥] Nikolaos Dimitratos,[§,∥] Lokesh Kesavan,[#] Peter P. Wells,[§,∥] Ralf Bechstein,[†] Henrik H. Jensen,[⊥] Stefan Wendt,[†] C. Richard A. Catlow,[§,∥] Christopher J. Kiely,[‡] Graham J. Hutchings,[∥,#,*] and Flemming Besenbacher[†,*]

[†]Interdisciplinary Nanoscience Center (iNANO) and Department of Physics and Astronomy, Aarhus University, Gustav Wieds Vej 14, DK-8000 Aarhus C, Denmark, [‡]Department of Materials Science and Engineering, Lehigh University, 5 East Packer Avenue, Bethlehem, Pennsylvania 18015-3195, United States, [§]Kathleen Lonsdale Materials Chemistry, Department of Chemistry, University College London, 20 Gordon Street, London, WC1H 0AJ, U.K., [⊥]Department of Chemistry, Aarhus University, Langelandsgade 140, DK-8000 Aarhus C, Denmark, [∥]The UK Catalysis Hub, Research Complex at Harwell, Rutherford Appleton Laboratory, Oxfordshire, OX11 0FA, U.K., and [#]Cardiff Catalysis Institute, School of Chemistry, Cardiff University, Cardiff, CF10 3AT, U.K.

ABSTRACT Photocatalytic hydrogen evolution may provide one of the solutions to the shift to a sustainable energy society, but the quantum efficiency of the process still needs to be improved. Precise control of the composition and structure of the metal nanoparticle cocatalysts is essential, and we show that fine-tuning the Au–Pd nanoparticle structure modifies the electronic properties of the cocatalyst significantly. Specifically, Pd_{shell}–Au_{core} nanoparticles immobilized on TiO_2 exhibit extremely high quantum efficiencies for H_2 production using a wide range of alcohols, implying that chemical byproducts from the biorefinery industry can be used as feedstocks. In addition, the excellent recyclability of our photocatalyst material indicates a high potential in industrial applications. We demonstrate that this particular elemental segregation provides optimal positioning of the unoccupied d-orbital states, which results in an enhanced utilization of the photoexcited electrons in redox reactions. We consider that the enhanced activity observed on TiO_2 is generic in nature and can be transferred to other narrow band gap semiconductor supports for visible light photocatalysis.

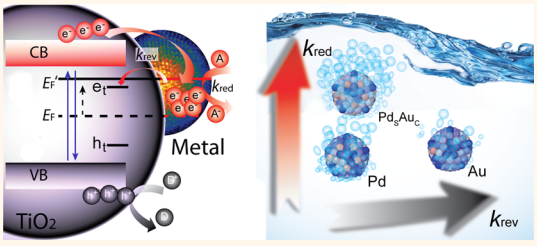

KEYWORDS: photocatalysis · hydrogen evolution · metal nanoparticles · cocatalysts · TiO_2 · density functional theory

Semiconductor photocatalysis has drawn great attention due to its environmental and energy conversion applications,[1,2] in particular for photocatalytic hydrogen (H_2) production,[3,4] which is considered a key element in our progress toward a hydrogen economy.[5] A number of materials (*i.e.*, TiO_2, CdS) capable of producing H_2 upon stimulation with suitable electromagnetic radiation have been identified.[6–8] However, their band structures are not entirely appropriate, and the corresponding rapid electron–hole recombination kinetics result in low quantum efficiencies; thus photocatalytic H_2 generation using these materials is not competitive with conventional H_2 production methods.[9] Combining the semiconductor with highly dispersed cocatalyst nanoparticles (NPs)[10,11] that spatially separate the photogenerated charge carriers is a feasible approach for enhancing the photocatalytic performance.[12–14]

Indeed, there are indications that the decoration of semiconductor particles with noble metal NPs is an effective way of achieving more efficient H_2 production.[3–8,12–21] However, most of these studies are focused on tuning the semiconductor materials, and the approach of using a metal cocatalyst is just simply adopted as an empirical procedure without knowing how and why the cocatalyst functions. Due to the high price of precious metals (*i.e.*, Au, Pd, and Pt), minimizing the metal cocatalyst loading while simultaneously improving the photocatalytic performance and stability of these materials is of vital importance in making these photocatalyst systems practical for large-scale H_2 production. These requirements call for a better understanding of the mechanistic role

* Address correspondence to hutch@cardiff.ac.uk (G. Hutchings), fbe@inano.au.dk (F. Besenbacher).

Received for review December 17, 2013 and accepted March 7, 2014.

Published online March 07, 2014
10.1021/nn500963m

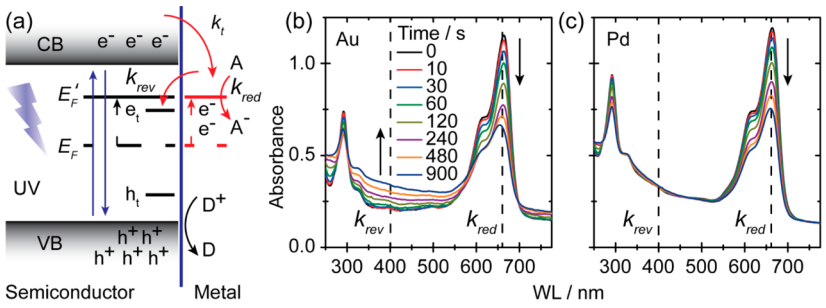

Figure 1. (a) Scheme of energy levels of the semiconductor−metal system under UV irradiation. E_F and E_F' represent the Fermi level of the system before and after irradiation. The trap states of excited electrons and holes are indicated as e_t and h_t. k_t, k_{red}, and k_{rev} denote the rate constants of the interfacial charge trapping (TiO_2 to metal), the reduction rate, and the reversed trapping rate (metal to TiO_2), respectively. A and A^- depict the electron acceptor and its reduced species; D and D^+ are the hole scavenger and its oxidized form. (b and c) *In situ* UV−vis absorption spectra of the photoinduced methylene blue (MB) reduction process under an N_2 atmosphere for monometallic Au and Pd NPs supported on TiO_2. Catalyst loadings were 50 mg/L.

of metal cocatalyst NPs and a synthesis technique that is capable of producing specially engineered "designer" metal NPs with an optimal set of structural and compositional characteristics.

The promotion effect of metal NPs can be qualitatively understood by considering the energy levels of the semiconductor−metal system (Figure 1a). The photoexcited electrons in the conduction band (CB) of a semiconductor can be rapidly transferred and trapped at the metal surface states, which results in the Fermi level (E_F) of the system shifting (E_F') toward the CB potential of the semiconductor.[10,11] The trapped electrons display a prolonged lifetime,[22] thus improving the efficiency of reduction reactions in the presence of proper electron acceptors (see "A" in Figure 1a).

Since the interfacial charge transfer of the electrons from metal NPs to the electron acceptors is a very slow process in comparison with the charge transfer from TiO_2 to metal NPs,[10] these accumulated electrons may get trapped *via* a reverse transportation process to the trap states (e_t) of the semiconductor. Therefore, an optimum performance requires a fast reduction reaction (high k_{red}) and a slow reverse transfer process (low k_{rev}) for the trapped photogenerated electrons. Unfortunately, k_{red} has been only seldom studied using model catalyst, and k_{rev} remains largely unknown due to the difficulty in probing the reverse charge transfer process. Thus, it is a crucial issue to probe k_{red} and k_{rev} of real semiconductor−metal systems at reaction conditions to assist the design and synthesis of highly efficient photocatalysts.

RESULTS AND DISCUSSION

We first examined the kinetics of trapped electrons on monometallic Au and Pd NPs supported on TiO_2 (Figures S1 and S2 in the Supporting Information) *in situ* by using methylene blue (MB) as a model probe molecule (Figure 1b and c, Figures S3−S8 in the Supporting Information).[23] The trapped electrons on Au and Pd NPs exhibit a more negative potential than that of a standard hydrogen electrode (SHE), which is capable of reducing MB (λ_{max} = 664 nm) to the colorless MB^{2-} species ($E_{MB/MB^{2-}}{}^0$ = 0.01 V *vs* SHE) under deaerated conditions.[10] Note that the photoreduction of MB is reversible in the presence of oxygen under dark conditions, which is a different situation compared to the photo-oxidation of MB in air (Figure S9 in the Supporting Information). The reduction rate constant, k_{red}, can be therefore derived from the MB evolution. As the UV−vis spectra were recorded *in situ*, the absorption of the TiO_2 (λ < 387 nm) and the scattering of the TiO_2 nanoparticles (λ > 387 nm) also contribute to the absorbance. Since a well-defined concentration of TiO_2 nanoparticle suspension yields a very stable baseline (see Figure S4 in the Supporting Information), the change of the baseline during the MB photoreduction can be associated with the reverse charge trapping of photogenerated electrons. Therefore, k_{rev} can be estimated from the absorbance change of the baseline (*i.e.*, at 400 nm), as a constant concentration was used in the experiment. Note that the trapping of excited electrons within crystalline TiO_2 can be neglected, and the increase in the baseline of the *in situ* UV−vis spectra can be solely correlated to the reverse trapping at the TiO_2 trap states (see Figure S4 in the Supporting Information). Interestingly, Au NPs deposited on TiO_2 gave large k_{red} and k_{rev}, whereas Pd-decorated TiO_2 showed a relatively small k_{red}, but a negligible k_{rev}. This result suggests that the charge-trapping and -releasing properties are governed by the electronic properties of the metal NPs.[22]

Since Pd most likely provides an ohmic contact, whereas Au shows capacitive properties,[10] we anticipated that both k_{red} and k_{rev} could be optimized by a deliberate control of compositional and structural properties of mixed Au−Pd NPs. Accordingly, we employed a colloidal method to synthesize a series of Au- and Pd-based NPs with a range of specific random alloy and core−shell configurations. These colloids were then supported on TiO_2 *via* a sol-immobilization process.[24] By adjusting the relative metal concentrations

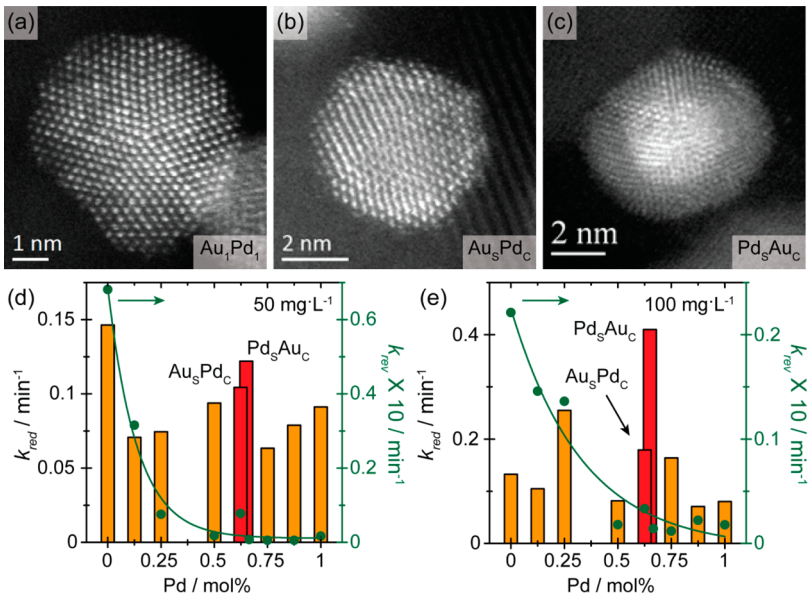

Figure 2. (a–c) Representative HAADF-STEM images of a Au_1Pd_1 random alloy particle, a Au_{shell}–Pd_{core} particle, and a Pd_{shell}–Au_{core} particle, respectively. (d and e) Rate constants k_{red} and k_{rev} as a function of the Pd concentration under constant irradiation (catalyst loading 50 mg/L) and insufficient irradiation (catalyst loading 100 mg/L), respectively. The metal loading was 1 wt % for all photocatalysts.

and co-reducing the metal precursors, well-dispersed Au–Pd random alloy NPs (Figure 2a) with tunable composition were prepared. By varying the addition sequence during the colloidal preparation, Au_{shell}–Pd_{core} ([Au_sPd_c], Figure 2b) and Pd_{shell}–Au_{core} ([Pd_sAu_c], Figure 2c) NPs were also prepared.[25] High angle annular dark field (HAADF) imaging showed that the metal NPs in all configurations are predominantly a mixture of multiply twinned icosahedral and untwinned cuboctahedral structures with occasional decahedral particles. Statistical analysis showed that all metal NPs with a 1:1 nominal Au:Pd molar ratio have a mean size of ~4–5 nm and a narrow size distribution (Figure S1 in the Supporting Information),[24,25] and the physical characteristics of the TiO_2 support were similar in all catalysts examined (Figure S2 in the Supporting Information).

Subsequently, we probed the kinetics of electrons trapped at metal NPs supported on TiO_2 under different irradiation conditions (Figures S5–S8 in the Supporting Information). By using a low catalyst loading (50 mg/L), we first examined the reaction kinetics under constant irradiation conditions (Figure 2d). We observed that an increase of the Pd content in the bimetallic NPs resulted in a ~33–50% reduction of k_{red}. However, k_{rev} also decreased exponentially with increasing Pd concentration and became negligible at an Au-to-Pd molar ratio of 1:1. Conversely, the core–shell structures, Au_sPd_c and Pd_sAu_c, maintained a relatively high k_{red} but very low k_{rev}. In addition, we also examined the kinetics under more realistic conditions (Figure 2e, Figures S6 and S7 in the Supporting Information). This was achieved by using a higher catalyst loading (100 mg/L), where the attenuation coefficient of the suspension and subsequently the full absorption path length of the photons were reduced. While the irradiation intensities for the exposed metal/TiO_2 nanoparticles remained unchanged in both cases (see Supporting Information), the photon flux became insufficient to illuminate all of the NPs in the suspension continuously in the case of the higher catalyst loading (100 mg/L). Thus, the experimental conditions have changed from "light-saturated" mode (50 mg/L) to a "catalyst-saturated" mode (100 mg/L). Similarly, a monotonic decay of k_{rev} was observed with increasing Pd content for the alloy NPs. Surprisingly, no obvious enhancement of k_{red} was observed for monometallic-, Au-, and Pd-rich (Au_7Pd_1 and Au_1Pd_7) and Au_1Pd_1 alloy NPs compared to the measurements for low catalyst loading. Since doubling the photocatalyst concentration did not change the photon flux densities encountered for individual NPs that were exposed to irradiation, it suggests that the electrons trapped at the surface sites of these particular NPs underwent rapid recombination under dark conditions (see Figures S5–S8, Movie S1, and detailed discussion in the Supporting Information). Conversely, the k_{red} of Au–Pd random alloys with molar ratios of 3:1 (25 mol % Pd) and 1:3 (75 mol % Pd) were significantly improved, underpinning the importance of fine-tuning the alloy composition and mean size for adjusting the recombination kinetics. The core–shell NPs, especially those with the Pd_sAu_c architecture, exhibited the optimum performance in extracting the trapped electrons to drive the desired reduction reactions.

As the reduction potential of the proton (E_{H^+}/H_2^0 = 0 V *vs* SHE) is very close to that of the MB reduction,

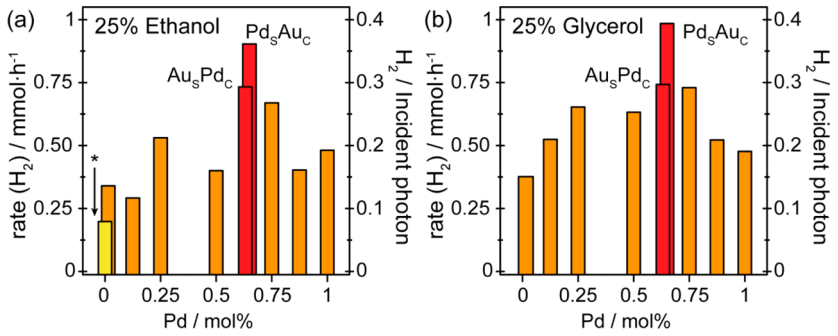

Figure 3. Photocatalytic H_2 production from (a) 25 vol % ethanol and (b) 25 vol % glycerol solutions using random alloys and core−shell Au−Pd NPs supported on TiO_2. The metal loading was 1 wt % for all photocatalysts. The reference material (marked as *) is a 1 wt % Au/TiO_2 prepared by using a standard photodeposition method.[6]

we expect optimization of k_{red} and k_{rev} *via* adjustment of the composition and structure of the metal NPs to be also beneficial for the photocatalytic H_2 evolution. Figure 3a depicts the H_2 evolution from a water−ethanol (25 vol%) solution. A conventional photodeposited Au/TiO_2 (marked as *ref**) catalyst was also evaluated for comparison.[6] For all photocatalytic testing of the different materials (Figures S10−S14 in the Supporting Information), the gas-phase products were primarily H_2 with trace amounts of CH_4, CO, and CO_2, whereas the liquid-phase products were CH_3CHO and CH_3COOH (Figure S15 and Table S2 in the Supporting Information), respectively. The sol-immobilized Au/TiO_2 catalyst showed a 1.7-fold increase in performance compared to the photodeposited Au/TiO_2, indicating that the preparation method has a significant effect on the structural characteristics of the catalyst (*e.g.*, the degree of contact between the metal and support, particle size control). According to our TEM analysis, an extended flat interface between each metal NP and the TiO_2 surface is achieved by the sol-immobilization approach,[24] resulting in a sufficient number of boundary sites that are essential for rapid charge transfer.

Furthermore, we found that the alloy composition and the morphology of the metal cocatalysts strongly influence the performance of the photocatalyst (Figure 3a and Figure S13 in the Supporting Information). Note that the photocatalytic H_2 evolution performances were strongly correlated to the kinetics of the trapped electrons. The TiO_2-supported Pd NPs showed a higher H_2 evolution rate compared to Au NPs, which agrees well with previous studies.[26,27] Both Au- and Pd-rich alloys (Au_7Pd_1 and Au_1Pd_7) exhibited a slightly decreased performance compared to that of their monometallic counterparts;, whereas the Au_1Pd_1 alloy NPs showed a performance that was approximately the average of the two monometallic supported catalysts. A strong synergistic effect was observed for Au−Pd alloys with molar ratios of 1:3 and 3:1 (see real-time Movie S1 in the Supporting Information). Interestingly, we also observed elevated H_2 evolution for the core−shell structure cocatalysts (Au_sPd_c and Pd_sAu_c) as compared to that displayed by random alloy NPs. According to a previous TEM analysis, the 3:1 and 1:3 random alloy NPs were found to have smaller mean particle sizes than either the 1:1 or the 7:1 and 1:7 random alloy NPs,[25] suggesting that metal particle size must also play an important role in determining the H_2 evolution efficiency. Most notably, the Pd_sAu_c/TiO_2 catalyst yielded a remarkable H_2 evolution rate of ~0.9 mmol·h^{-1}, which corresponds to a quantum efficiency of ~0.35 H_2 molecules per incident photon, *i.e.*, an apparent quantum efficiency (AQE) of ~70%. This exceptionally high efficiency displayed by the Pd_sAu_c/TiO_2 catalyst is superior to that of any photocatalyst reported to date using renewable organic chemicals as scavengers (Table 1). In addition, high quantum efficiency values can be obtained over a wide operation window of ethanol concentrations, which allows the use of waste alcohols as a feedstock (Table S1 in the Supporting Information).

We have further evaluated our photocatalysts using glycerol as the scavenger (Figure 3b), which is a low-value byproduct from the biorefinery industry. Significantly, a similar promotion trend was observed, and the Pd_sAu_c/TiO_2 system again yielded an impressive AQE of ~78% (0.39 H_2/photon; see real-time Movie S2 in the Supporting Information), which suggests that the kinetics of the trapped electrons on our designer metal−TiO_2 systems show a general trend and may be applicable to other reactions. Moreover, a whole series of other bioavailable chemical products (*e.g.*, ethylene glycol, 1,2-propanediol, glucose, and fructose) and especially crude glycerol from a biorefinery can also be used as feedstocks for photocatalytic H_2 production with high quantum efficiencies, as shown in Figure 4a. This demonstrates the excellent versatility and the great potential of our Pd_sAu_c/TiO_2 photocatalyst for large-scale applications.

We have also assessed the reusability of the Pd_sAu_c/TiO_2 photocatalyst (Figure 4b and Figure S14 in the Supporting Information) and observed a stable catalytic performance for H_2 evolution over nine consecutive cycles without any recovery treatment. Since a 2 h UV irradiation was conducted for each cycle, we calculated that ~0.36 L of H_2 gas was produced over the course

TABLE 1. Comparison of our Pd_sAu_c/TiO_2 Photocatalyst with Other Promising Photocatalysts for Their Apparent Quantum Efficiencies for H_2 Production

catalyst	AQE[a]/%	rate	light source	scavenger
1 wt % Pd_sAu_c/TiO_2 (this work)	78	19.6 mol·kg^{-1}h^{-1} ~1.6 mol·m^{-2} h^{-1}[b]	UV	25 vol % glycerol
V_2O_5 film[28]	38.7	0.8 mol·m^{-2} h^{-1}	UV	20 vol % EtOH
Pt/TiO_2 film[29]	37	0.03 mol·m^{-2} h^{-1}[b]	UV	80 vol % EtOH
		5.6 mol·kg^{-1} h^{-1}[b]		
1 wt % Pt-$BaTi_4O_9$[30]	11.7	8.5 mol·kg^{-1} h^{-1}	UV	20 vol % EtOH
0.5 wt % Pt-polypyrrole-TiO_2[16]	10.6	7.6 mol·kg^{-1} h^{-1}	UV	0.1 vol % MeOH
4 wt % Au/TiO_2[13]	~3[b]	6.9 mol·kg^{-1} h^{-1}[b]	UV	30 vol % EtOH
1 wt % PtO/TiO_2[19]	N/A	4.4 mol·kg^{-1} h^{-1}[b]	UV	30 vol % MeOH

[a] AQE refers to apparent quantum efficiency as calculated using the following equation:

$$\text{AQE} = 2n(H_2)/n(\text{incident photons})$$

[b] Estimated values.

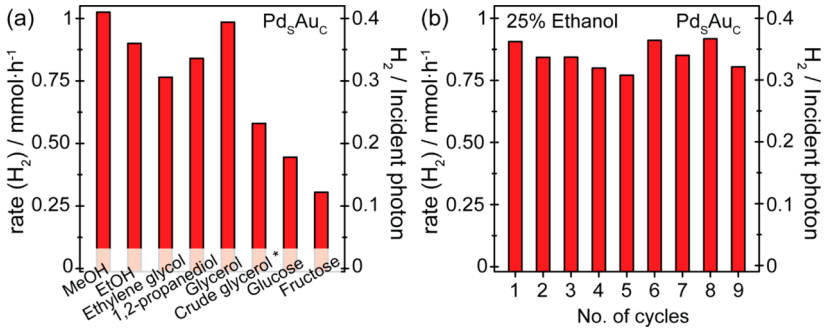

Figure 4. (a) Photocatalytic H_2 production from a variety of other biorefinery "waste" chemicals. The concentrations of glucose and fructose solutions used were 25 wt %, whereas the rest were 25 vol %. Prior to the test, the crude glycerol received from biodiesel refinery was separated to remove the organic layer, filtered through activated carbon, treated with a cation exchange resin, and treated again with activated carbon. (b) Durability of the Pd_sAu_c supported on TiO_2 catalyst using 25 vol % ethanol solution. The photocatalyst was reused directly after each measurement.

of the whole reusability test from 25 mL of ethanol solution with an apparent irradiation area of only 12.6 cm^2. This corresponds to a turnover number of ~9400 for the Pd_SAu_C nanoparticles as the metal loading was 1 wt % (~1.7 μmol $Pd_{shell}Au_{core}$), implying that we have a robust photocatalytic process.

Recent theoretical work on AuPd nanoalloys has focused on the thermodynamic preference toward the surface segregation of Au,[31−33] with the surface segregation of Pd being attributed to environmental effects[34,35] as seen for bulk (100) surfaces under reducing environments.[36] Experimental accounts have illustrated the robust stability of $Au_{core}-Pd_{shell}$ and $Pd_{core}-Au_{shell}$ when synthesized *via* chemical methods,[24,37−40] with the elemental distribution for gas-phase and supported core−shell structures stable up to ~500 K in experiment and theory,[24,39,41−43] well above the ambient temperatures employed in our experiments. However, previous work has considered neither the electronic properties of the different NP elemental configurations, which would be important for understanding the ability to trap photoexcited electrons and effects on photocatalytic performance, nor the natural alignment of electron levels in NPs with the band structure of a semiconducting substrate, which would provide insight into the favorability of the transfer of photoexcited electrons from the substrate to the NP.

Therefore, we calculated the electronic properties of Au, Pd, and bimetallic core−shell clusters using density functional theory (DFT) to gain insight into how the morphology and the elemental distribution of the NPs alter the electronic properties. Icosahedral (I_h), cuboctahedral (*CO*), and ino-decahedral ($I\text{-}D_h$) structures (Figure S16 in Supporting Information) were chosen, as these particular morphologies correspond to the structures identified by STEM observation.[22] The size of the NPs was set to 147 atoms for calculations, as the properties for this nuclearity were found to be extendable toward the experimental sizes (Figure S17 in the Supporting Information).

The extracted density of states (DOS) for I_h Au and I_h Pd clusters (Figure 5a and 5b) reveal that many more unoccupied states lay just above E_F in the case of the I_h Pd cluster, which would be favorable for the trapping of electrons and performing redox reactions. The natural alignment of the NP DOS with the conduction band for TiO_2 shows that photoexcited electrons

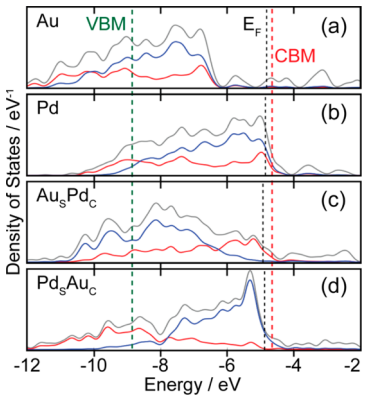

Figure 5. (a–d) Electronic density of states (DOS) profiles of 147-atom icosahedral clusters of Au, Pd, Au_sPd_c, and Pd_sAu_c, respectively. The total valence DOS (gray) is complemented by the contributions of the d-orbitals in both the core (red) and outer shell (blue) region. E_F of the metal clusters, conduction band minima (CBM), and valence band maxima (VBM) of TiO_2 are indicated by black and red dashed lines, respectively.[44]

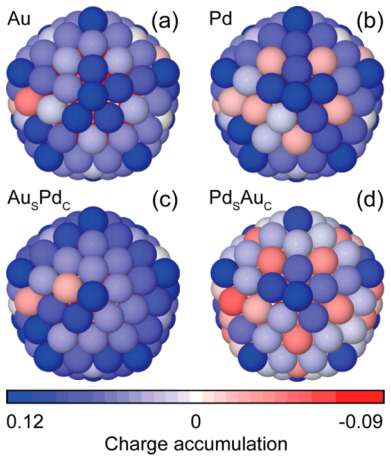

Figure 6. (a–d) Charge localization from the view of the (100) surface of 147-atom icosahedral clusters of Au, Pd, Au_sPd_c, and Pd_sAu_c, respectively. The blue and red colors represent atoms with electron accumulation and depletion, respectively.

would benefit energetically from transferring to the metallic NP, as the E_F of the NPs sits below the conduction band minimum (CBM) of TiO_2.[44] Moreover, for the bimetallic core–shell structures, the number of unoccupied surface states just above the E_F increases with surface Pd concentration: orbital analysis on the I_h Pd_sAu_c NP shows that >60% of all states just above the Fermi level are surface-localized d-orbitals, compared to <8% for the Au_sPd_c NP (Figure 5c). In both cases, the E_F remains below the CBM of TiO_2 for the bimetallic NPs. These unoccupied, energetically favorable, and physically accessible surface d-orbitals on the Pd_sAu_c NPs (Figure 5d) are deemed highly beneficial for extending the lifetime of the photoexcited states transferred from the conduction band of TiO_2.[44] The observed trends in electronic structure were found to be consistent for both the *I-D*$_h$ and *CO* structures as well (Figure S18 in the Supporting Information).

In addition, we assessed the net charge localization on the surface of the icosahedral-structured NPs, to rationalize the beneficial properties for the reduction process. On Au, Pd, and Au_sPd_c NPs (Figure 6a–d), net electron accumulation (indicated by blue atoms) predominantly occurs throughout the shell, whereas for the Pd_sAu_c NPs a net accumulation of charge occurs primarily on the vertex sites (Figure 6d). Most noticeably, charge depletion is prominent for the core regions of all NPs except in the case of Pd_sAu_c, as a result of the electronegative and capacitive properties of its Au core. Similar trends were observed for *CO* and *I-D*$_h$ structures (Figure S19 in the Supporting Information) and occur over a range of sizes, suggesting that the reduced surface accumulation of electrons for Pd_sAu_c NPs facilitates the storage and release of photoexcited electrons for catalysis.

CONCLUSIONS

We have probed the kinetics of the photogenerated electrons on real metal–semiconductor photocatalyst systems and revealed the importance of optimizing the electronic properties of the metal cocatalyst NP component in heterogeneous photocatalysts. In particular, by fine-tuning the composition and structure of the metal NPs, we have identified Pd_{shell}–Au_{core} NPs supported on TiO_2 to have extraordinarily high efficiencies for the photocatalytic H_2 evolution over a variety of important feedstock chemicals, even purified crude glycerol from biorefinery. Further investigation of the substrate–NP interactions and electron transfer across the substrate–NP interface should provide a clearer understanding of the role that metal NPs have in cocatalyzed photocatalytic reactions. Furthermore we believe that the deliberately designed cocatalyst approach is applicable to other metal–support combinations and will allow for the tailored fabrication of next-generation hybrid photocatalyst materials that are optimized for large-scale applications.

EXPERIMENTAL SECTION

Synthesis and Characterization of Photocatalysts. Metal nanoparticles were prepared and supported on TiO_2 (Degussa P25) using a sol-immobilization method. Monometallic Au, Pd, and three distinct Au–Pd sols were prepared by controlling the metal salt identity and adding sequences. $PdCl_2$, $HAuCl_4 \cdot 3H_2O$ (Johnson Matthey), poly(vinyl alcohol) (PVA) (Aldrich, MW = 10 000, 80% hydrolyzed), and $NaBH_4$ were used as reagents. Immobilization of the sols was accomplished by adding TiO_2 (acidified at pH 1 by sulfuric acid) after 30 min of sol-generation under vigorous stirring conditions. The total metal loading was maintained at 1% wt. The as-prepared photocatalysts were

filtered, washed thoroughly with distilled water (neutral mother liquors), and dried at 120 °C for 16 h. The catalysts were prepared for TEM/STEM analysis by dry dispersing the catalyst powder onto a holey carbon TEM grid. HREM and HAADF imaging experiments were carried out using a 200 kV JEOL 2200FS transmission electron microscope equipped with a CEOS probe aberration corrector. All the STEM-HAADF images were treated with a light low pass filter using a 3 × 3 kernel to decrease the high-frequency noise (Figure S1 in the Supporting Information). The X-ray diffraction (XRD) patterns of selected samples were measured using powder X-ray diffractometer (PXRD, Stadi P, Stoe) with Cu Kα radiation from a curved Ge(111) monochromator (Figure S2 in the Supporting Information). The surface areas of selected samples were determined by the Brunauer–Emmett–Teller (BET) method using N_2 adsorption isotherms at 77 K by a surface area analyzer (Quantachrome NOVA 2000). The samples were degassed 5 h at 393 K in a vacuum oven before BET measurements (Figure S2 in the Supporting Information).

Photocatalytic Characterizations. A UV LED (365 nm, Optimax 365) with a photon flux of 4×10^{17} photons/s was used in all experiments (Figure S3 in the Supporting Information). The kinetics of photogenerated electrons was probed by following the photoreduction of MB under N_2-saturated conditions. Suspensions with different loadings (50 and 100 mg/L) of the as-synthesized catalyst sample were UV cleaned for 2 h prior to the addition of MB solution. Then 1 mL of MB (500 μM) was dropped into the suspension and subsequently purged with N_2 continuously for 30 min prior to photoinduced reduction of MB. Meanwhile, the suspension was circulated *via* a peristaltic pump through a sealed flow cuvette placed in a UV–vis spectrometer (UV-1800, Shimadzu). The UV irradiation was then commenced when the MB adsorption equilibrium was reached. UV–vis spectra were recorded *in situ* at given time intervals for all samples. The photocatalytic H_2 production using various chemical feedstocks as sacrificial reagents was carried out in a leak-tight reactor connected to a mass spectrometer (Hiden HPR-20). The catalyst–water suspension (2 g/L) was prepared and cleaned by UV irradiation for 2 h to remove the PVA ligand prior to the experiment. A desired amount of sacrificial reagents (methanol, ethanol, ethylene glycol, glycerol, filtered crude glycerol, 1,2-propanediol, glucose, or fructose) was then added to the reactor. The total liquid volume was always adjusted to be 25 mL. Details of the hydrogen evolution measurement system, experimental protocol, calculation, and calibration of the H_2 signals were described in the Supporting Information. The liquid products were measured by a nuclear magnetic resonance (NMR, Varian 400), and the analysis procedure and NMR spectra were presented in the Supporting Information.

Theoretical Calculations. The nanoparticles were modeled as icosahedral, cuboctahedral, and ino-decahedral structures, as these proved to be the most suitable match to the STEM images in this and previous work.[24] The number of atoms (*N*) required for the formation of these NPs with geometrically complete shells and negligible quantum effects is found to be 147 according to our calculations. All DFT calculations were performed using the projector-augmented wave method as implemented in the software package GPAW,[45] using the PBE exchange–correlation functional,[46] a real-space grid spacing of 0.18 Å, and Fermi–Dirac occupation smearing of 0.1 eV. Relativistic effects are included in the PAW configurations. Each of the NPs was relaxed until all forces on the atoms were below 0.01 eV/Å before determining the density of states and quantifying the level of charge redistribution within the NPs.[47]

Conflict of Interest: The authors declare no competing financial interest.

Acknowledgment. The authors acknowledge the Center of Energy Materials (CEM), the Danish Strategic Research Council, the Carlsberg Foundation, the EPSRC, the UK's HPC Materials Chemistry Consortium (EPSRC, EP/F067496), and NSF for financial support.

Supporting Information Available: The sample preparation and characterization, quantum efficiency and reusability evaluation, products analysis, and DFT calculations are available free of charge *via* the Internet at http://pubs.acs.org.

REFERENCES AND NOTES

1. In, S.-I.; Vaughn, D. D., II; Schaak, R. E. Hybrid CuO-TiO_2-xNx Hollow Nanocubes for Photocatalytic Conversion of CO_2 into Methane under Solar Irradiation. *Angew. Chem., Int. Ed.* **2012**, *51*, 3915–3918.
2. Henderson, M. A. A Surface Science Perspective on TiO_2 Photocatalysis. *Surf. Sci. Rep.* **2011**, *66*, 185–297.
3. Chen, X. B.; Liu, L.; Yu, P. Y.; Mao, S. S. Increasing Solar Absorption for Photocatalysis with Black Hydrogenated Titanium Dioxide Nanocrystals. *Science* **2011**, *331*, 746–750.
4. Silva, C. G.; Juarez, R.; Marino, T.; Molinari, R.; Garcia, H. Influence of Excitation Wavelength (UV or Visible Light) on the Photocatalytic Activity of Titania Containing Gold Nanoparticles for the Generation of Hydrogen or Oxygen from Water. *J. Am. Chem. Soc.* **2011**, *133*, 595–602.
5. Chen, X.; Shen, S.; Guo, L.; Mao, S. S. Semiconductor-Based Photocatalytic Hydrogen Generation. *Chem. Rev.* **2010**, *110*, 6503–6570.
6. Bamwenda, G. R.; Tsubota, S.; Nakamura, T.; Haruta, M. Photoassisted Hydrogen-Production from a Water-Ethanol Solution - A Comparison of Activities of Au-TiO_2 and Pt-TiO_2. *J. Photochem. Photobiol., A* **1995**, *89*, 177–189.
7. Bao, N.; Shen, L.; Takata, T.; Domen, K. Self-Templated Synthesis of Nanoporous CdS Nanostructures for Highly Efficient Photocatalytic Hydrogen Production under Visible Light. *Chem. Mater.* **2007**, *20*, 110–117.
8. Maeda, K.; Teramura, K.; Lu, D. L.; Saito, N.; Inoue, Y.; Domen, K. Noble-Metal/Cr_2O_3 Core/Shell Nanoparticles as a Cocatalyst for Photocatalytic Overall Water Splitting. *Angew. Chem., Int. Ed.* **2006**, *45*, 7806–7809.
9. Häussinger, P.; Lohmüller, R.; Watson, A. M. *Ullmann's Encyclopedia of Industrial Chemistry*; Wiley-VCH Verlag GmbH & Co. KGaA, 2000.
10. Takai, A.; Kamat, P. V. Capture, Store, and Discharge. Shuttling Photogenerated Electrons across TiO_2-Silver Interface. *ACS Nano* **2011**, *5*, 7369–7376.
11. Cozzoli, P. D.; Curri, M. L.; Agostiano, A. Efficient Charge Storage in Photoexcited TiO_2 Nanorod-Noble Metal Nanoparticle Composite Systems. *Chem. Commun.* **2005**, 3186–3188.
12. Maeda, K.; Higashi, M.; Lu, D. L.; Abe, R.; Domen, K. Efficient Nonsacrificial Water Splitting through Two-Step Photoexcitation by Visible Light Using a Modified Oxynitride as a Hydrogen Evolution Photocatalyst. *J. Am. Chem. Soc.* **2010**, *132*, 5858–5868.
13. Murdoch, M.; Waterhouse, G. I. N.; Nadeem, M. A.; Metson, J. B.; Keane, M. A.; Howe, R. F.; Llorca, J.; Idriss, H. The Effect of Gold Loading and Particle Size on Photocatalytic Hydrogen Production from Ethanol over Au/TiO_2 Nanoparticles. *Nat. Chem.* **2011**, *3*, 489–492.
14. Yang, J.; Wang, D.; Han, H.; Li, C. Roles of Cocatalysts in Photocatalysis and Photoelectrocatalysis. *Acc. Chem. Res.* **2013**, *46*, 1900–1909.
15. Mizukoshi, Y.; Sato, K.; Konno, T. J.; Masahashi, N. Dependence of Photocatalytic Activities upon the Structures of Au/Pd Bimetallic Nanoparticles Immobilized on TiO_2 Surface. *Appl. Catal., B* **2010**, *94*, 248–253.
16. Kandiel, T. A.; Dillert, R.; Bahnemann, D. W. Enhanced Photocatalytic Production of Molecular Hydrogen on TiO_2 Modified with Pt-polypyrrole Nanocomposites. *Photochem. Photobiol. Sci.* **2009**, *8*, 683–690.
17. Naldoni, A.; D'Arienzo, M.; Altomare, M.; Marelli, M.; Scotti, R.; Morazzoni, F.; Selli, E.; Dal Santo, V. Pt and Au/TiO_2 Photocatalysts for Methanol Reforming: Role of Metal Nanoparticles in Tuning Charge Trapping Properties and Photoefficiency. *Appl. Catal., B* **2013**, *130*, 239–248.
18. Chiarello, G. L.; Selli, E.; Forni, L. Photocatalytic Hydrogen Production over Flame Spray Pyrolysis-Synthesised TiO_2 and Au/TiO_2. *Appl. Catal., B* **2008**, *84*, 332–339.
19. Hang Li, Y.; Xing, J.; Jia Chen, Z.; Li, Z.; Tian, F.; Rong Zheng, L.; Feng Wang, H.; Hu, P.; Jun Zhao, H.; Gui Yang, H. Unidirectional Suppression of Hydrogen Oxidation on Oxidized Platinum Clusters. *Nat. Commun.* **2013**, *4*, 2500–2507.

20. Cheng, M. H.; Zhu, M. S.; Du, Y. K.; Yang, P. Enhanced Photocatalytic Hydrogen Evolution Based on Efficient Electron Transfer in Triphenylamine-Based Dye Functionalized Au@Pt Bimetallic Core/Shell Nanocomposite. *Int. J. Hydrogen Energy* **2013**, *38*, 8631–8638.
21. Rawalekar, S.; Mokari, T. Rational Design of Hybrid Nanostructures for Advanced Photocatalysis. *Adv. Energy Mater.* **2013**, *3*, 12–27.
22. Subramanian, V.; Wolf, E. E.; Kamat, P. V. Catalysis with TiO_2/Gold Nanocomposites. Effect of Metal Particle Size on the Fermi Level Equilibration. *J. Am. Chem. Soc.* **2004**, *126*, 4943–4950.
23. Su, R.; Tiruvalam, R. C.; He, Q.; Dimitratos, N.; Kesavan, L.; Hammond, C.; Lopez-Sanchez, J. A.; Bechstein, R.; Kiely, C. J.; Hutchings, G. J.; *et al*. Promotion of Phenol Photodecomposition over TiO_2 Using Au, Pd, and Au-Pd Nanoparticles. *ACS Nano* **2012**, *6*, 6284–6292.
24. Tiruvalam, R. C.; Pritchard, J. C.; Dimitratos, N.; Lopez-Sanchez, J. A.; Edwards, J. K.; Carley, A. F.; Hutchings, G. J.; Kiely, C. J. Aberration Corrected Analytical Electron Microscopy Studies of Sol-immobilized Au plus Pd, Au{Pd}, and Pd{Au} Catalysts Used for Benzyl Alcohol Oxidation and Hydrogen Peroxide Production. *Faraday Discuss.* **2011**, *152*, 63–86.
25. Pritchard, J.; Kesavan, L.; Piccinini, M.; He, Q.; Tiruvalam, R.; Dimitratos, N.; Lopez-Sanchez, J. A.; Carley, A. F.; Edwards, J. K.; Kiely, C. J.; *et al*. Direct Synthesis of Hydrogen Peroxide and Benzyl Alcohol Oxidation Using Au-Pd Catalysts Prepared by Sol Immobilization. *Langmuir* **2010**, *26*, 16568–16577.
26. Al-Mazroai, L. S.; Bowker, M.; Davies, P.; Dickinson, A.; Greaves, J.; James, D.; Millard, L. The Photocatalytic Reforming of Methanol. *Catal. Today* **2007**, *122*, 46–50.
27. Mizukoshi, Y.; Makise, Y.; Shuto, T.; Hu, J.; Tominaga, A.; Shironita, S.; Tanabe, S. Immobilization of Noble Metal Nanoparticles on the Surface of TiO_2 by the Sonochemical Method: Photocatalytic Production of Hydrogen from an Aqueous Solution of Ethanol. *Ultrason. Sonochem.* **2007**, *14*, 387–392.
28. Sun, W.; Zhang, S. Q.; Wang, C.; Liu, Z. X.; Mao, Z. Q. Effects of Cocatalyst and Calcination Temperature on Photocatalytic Hydrogen Evolution over $BaTi_4O_9$ Powder Synthesized by The Polymerized Complex Method. *Catal. Lett.* **2008**, *123*, 282–288.
29. Wang, Y. Q.; Zhang, Z. J.; Zhu, Y.; Li, Z. C.; Vajtai, R.; Ci, L. J.; Ajayan, P. M. Nanostructured VO_2 Photocatalysts for Hydrogen Production. *ACS Nano* **2008**, *2*, 1492–1496.
30. Strataki, N.; Bekiari, V.; Kondarides, D. I.; Lianos, P. Hydrogen Production by Photocatalytic Alcohol Reforming Employing Highly Efficient Nanocrystalline Titania Films. *Appl. Catal., B* **2007**, *77*, 184–189.
31. Bruma, A.; Ismail, R.; Paz-Borbon, L. O.; Arslan, H.; Barcaro, G.; Fortunelli, A.; Li, Z. Y.; Johnston, R. L. DFT Study of the Structures and Energetics of 98-Atom AuPd Clusters. *Nanoscale* **2013**, *5*, 646–652.
32. Logsdail, A. J.; Johnston, R. L. Interdependence of Structure and Chemical Order in High Symmetry $(PdAu)_N$ Nanoclusters. *RSC Adv.* **2012**, *2*, 5863–5869.
33. Pittaway, F.; Paz-Borbon, L. O.; Johnston, R. L.; Arslan, H.; Ferrando, R.; Mottet, C.; Barcaro, G.; Fortunelli, A. Theoretical Studies of Palladium-Gold Nanoclusters: Pd-Au Clusters with up to 50 Atoms. *J. Phys. Chem. C* **2009**, *113*, 9141–9152.
34. Cheng, D.; Atanasov, I. S.; Hou, M. Influence of the Environment on Equilibrium Properties of Au-Pd Clusters. *Eur. Phys. J. D* **2011**, *64*, 37–44.
35. West, P. S.; Johnston, R. L.; Barcaro, G.; Fortunelli, A. The Effect of CO and H Chemisorption on the Chemical Ordering of Bimetallic Clusters. *J. Phys. Chem. C* **2010**, *114*, 19678–19686.
36. Gao, F.; Wang, Y. L.; Goodman, D. W. CO Oxidation over AuPd(100) from Ultrahigh Vacuum to Near-Atmospheric Pressures: CO Adsorption-Induced Surface Segregation and Reaction Kinetics. *J. Phys. Chem. C* **2009**, *113*, 14993–15000.
37. Lee, Y. W.; Kim, M.; Kim, Z. H.; Han, S. W. One-Step Synthesis of Au@Pd Core-Shell Nanooctahedron. *J. Am. Chem. Soc.* **2009**, *131*, 17036–17037.
38. Ferrer, D.; Torres-Castro, A.; Gao, X.; Sepulveda-Guzman, S.; Ortiz-Mendez, U.; Jose-Yacaman, M. Three-Layer Core/Shell Structure in Au-Pd Bimetallic Nanoparticles. *Nano Lett.* **2007**, *7*, 1701–1705.
39. Liu, H. B.; Pal, U.; Medina, A.; Maldonado, C.; Ascencio, J. A. Structural Incoherency and Structure Reversal in Bimetallic Au-Pd Nanoclusters. *Phys. Rev. B* **2005**, *71*, 075403.
40. Hu, J. W.; Zhang, Y.; Li, J. F.; Liu, Z.; Ren, B.; Sun, S. G.; Tian, Z. Q.; Lian, T. Synthesis of Au@Pd Core-Shell Nanoparticles with Controllable Size and Their Application in Surface-Enhanced Raman Spectroscopy. *Chem. Phys. Lett.* **2005**, *408*, 354–359.
41. Mejía-Rosales, S. J.; Fernández-Navarro, C.; Pérez-Tijerina, E.; Montejano-Carrizales, J. M.; José-Yacamán, M. Two-Stage Melting of Au−Pd Nanoparticles. *J. Phys. Chem. B* **2006**, *110*, 12884–12889.
42. Mejía-Rosales, S. J.; Fernández-Navarro, C.; Pérez-Tijerina, E.; Blom, D. A.; Allard, L. F.; José-Yacamán, M. On the Structure of Au/Pd Bimetallic Nanoparticles. *J. Phys. Chem. C* **2006**, *111*, 1256–1260.
43. Rodríguez-López, J. L.; Montejano-Carrizales, J. M.; Pal, U.; Sánchez-Ramírez, J. F.; Troiani, H. E.; García, D.; Miki-Yoshida, M.; José-Yacamán, M. Surface Reconstruction and Decahedral Structure of Bimetallic Nanoparticles. *Phys. Rev. Lett.* **2004**, *92*, 196102.
44. Scanlon, D. O.; Dunnill, C. W.; Buckeridge, J.; Shevlin, S. A.; Logsdail, A. J.; Woodley, S. M.; Catlow, C. R. A.; Powell, M. J.; Palgrave, R. G.; Parkin, I. P.; *et al*. Band Alignment of Rutile and Anatase TiO_2. *Nat. Mater.* **2013**, *12*, 798–801.
45. Enkovaara, J.; Rostgaard, C.; Mortensen, J. J.; Chen, J.; Dulak, M.; Ferrighi, L.; Gavnholt, J.; Glinsvad, C.; Haikola, V.; Hansen, H. A.; *et al*. Electronic Structure Calculations with GPAW: A Real-Space Implementation of the Projector Augmented-Wave Method. *J. Phys.: Condens. Matter* **2010**, *22*, 253202.
46. Perdew, J. P.; Burke, K.; Ernzerhof, M. Generalized Gradient Approximation Made Simple. *Phys. Rev. Lett.* **1996**, *77*, 3865–3868.
47. Wang, T.; Sanville, E.; Henkelman, G. A Grid-Based Bader Analysis Algorithm without Lattice Bias. *J. Phys.: Condens. Matter* **2009**, *21*, 084204.